

First-principles investigation of magnetic and transport properties in hole-doped shandite compounds $\text{Co}_3\text{In}_x\text{Sn}_{2-x}\text{S}_2$

Yuki Yanagi¹, Junya Ikeda², Kohei Fujiwara², Kentaro Nomura^{2,3}, Atsushi Tsukazaki^{2,3,4} and Michi-To Suzuki^{1,5}
¹*Center for Computational Materials Science, Institute for Materials Research, Tohoku University, Sendai, Miyagi, 950-8577, Japan*

²*Institute for Materials Research, Tohoku University, Sendai Miyagi 950-8577, Japan*

³*Center for Spintronics Research Network, Tohoku University, Sendai, Miyagi 980-8577, Japan*

⁴*Center for Science and Innovation in Spintronics (CSIS),*

Core Research Cluster, Tohoku University, Sendai, Miyagi 980-8577, Japan

⁵*Center for Spintronics Research Network, Graduate School of Engineering Science, Osaka University, Toyonaka, Osaka 560-8531, Japan*

Co-based shandite $\text{Co}_3\text{Sn}_2\text{S}_2$ is a representative example of magnetic Weyl semimetals showing rich transport phenomena. We thoroughly investigate magnetic and transport properties of hole-doped shandites $\text{Co}_3\text{In}_x\text{Sn}_{2-x}\text{S}_2$ by first-principles calculations. The calculations reproduce nonlinear reduction of anomalous Hall conductivity with doping In for $\text{Co}_3\text{Sn}_2\text{S}_2$, as reported in experiments, against the linearly decreased ferromagnetic moment within virtual crystal approximation. We show that a drastic change in the band parity character of Fermi surfaces, attributed to the nodal rings lifted energetically with In-doping, leads to strong enhancement of anomalous Nernst conductivity with reversing its sign in $\text{Co}_3\text{In}_x\text{Sn}_{2-x}\text{S}_2$.

I. INTRODUCTION

Novel charge and spin transports have attracted growing interests in the contexts of topological phases of matter. The anomalous Hall effect (AHE) and anomalous Nernst effect (ANE) are classical examples of such phenomena and have been studied for many years [1]. The AHE (ANE) is characterized by a transverse charge current flow \mathbf{j} induced by an applied electric field \mathbf{E} (thermal gradient ∇T) in the absence of an external magnetic field as follows,

$$j_a = \sum_b \left[\sigma_{ab}^A E_b + \alpha_{ab}^A (-\nabla_b T) \right], \quad (1)$$

where antisymmetric tensors σ_{ab}^A and α_{ab}^A are anomalous Hall conductivity (AHC) and anomalous Nernst conductivity (ANC), respectively, with $a, b = x, y, z$. Since the AHC and ANC are closely related to topological properties of electronic structures via Berry curvature [1–5], significant effort has been devoted to exploring such anomalous transports in topological quantum matters with time-reversal symmetry breaking. Recently, large anomalous Hall and Nernst responses have been observed in magnetic Weyl semimetals including $\text{Co}_3\text{Sn}_2\text{S}_2$ and Co_2MnGa [6–10].

Shandite compound $\text{Co}_3\text{Sn}_2\text{S}_2$ is a half-metallic ferromagnet with transition temperature $T_c \sim 177$ K and saturated moment $M \sim 0.3 \mu_B$ per Co atom [11–14]. This material is a representative example of magnetic Weyl semimetals since, according to the angle resolved photoemission spectroscopy (ARPES) and electronic structure calculations, Weyl nodes are located near the Fermi energy [6, 7, 15]. In Weyl semimetals, the divergent behavior of the Berry curvature at the Weyl nodes can give rise to characteristic physics, e.g., the chiral magnetic effect and the emergence of the anomalous surface states called Fermi arcs [3]. The existence of the anomalous surface states in $\text{Co}_3\text{Sn}_2\text{S}_2$ has been confirmed by the ARPES and scanning tunneling spectroscopy (STS) measurements [15–17], supporting the existence of the Weyl nodes near the Fermi energy.

$\text{Co}_3\text{Sn}_2\text{S}_2$ is expected to be a potential candidate for the thermoelectric device applications due to the characteristic transport phenomena with the large AHC and ANC, reaching $\sigma_{xy}^A \sim 500\text{--}1130 \text{ S cm}^{-1}$ [6, 7] and $\alpha_{xy}^A \sim 2\text{--}10 \text{ A K}^{-1} \text{ m}^{-1}$ [8, 18], respectively. Previous theoretical studies imply the close relation between these anomalous transports and topological bands such as Weyl nodes and nodal rings [1–3, 5–7, 19–21]. Controlling pressure, temperature and chemical composition often affect transport properties. It is known that, in $\text{Co}_3\text{Sn}_2\text{S}_2$, applying pressure suppresses the AHE, leading to the AHC and Hall angle comparable to those in conventional ferromagnetic metals [22–24].

It has also been shown experimentally that the chemical substitution have a considerable impact on the magnetic and transport properties. So far, the effects of substitution of Fe and Ni for Co and of In for Sn have been investigated [11, 25–29], where Ni substitution corresponds to the electron doping, while Fe and In substitutions correspond to the hole doping. Irrespective of doped elements, similar doping dependence of magnetic properties has been confirmed, that is, the monotonic decrease of the transition temperature and magnetic moment with increasing doping content. The doping effects on transport properties, on the other hand, show more complicated behaviors. In the case of the Ni substitution, the AHC decreases monotonically with the doping content [28], while in the cases of Fe and In substitutions, AHC is enhanced for relatively small doping and decreases for large doping [27, 29]. From the theoretical side, the effects of substitution atoms on magnetic properties and/or electric transport properties have been previously investigated based on the first-principles calculations with the supercell approach for specific doping concentrations [26–28, 30]. A systematic investigation of the atom substitution effects on the thermoelectric transport, i.e., Nernst effect has not been performed. Here, we present a systematic investigation of the effects of In-doping into Sn sites on the thermoelectric transports as well as magnetic properties based on the first-principles method.

II. METHODS

We perform the density functional calculation for $\text{Co}_3\text{In}_x\text{Sn}_{2-x}\text{S}_2$ by using the WIEN2K code [31, 32]. Sn/In substitution effects are treated within the virtual crystal approximation (VCA) and with the lattice parameters adopted from the experimental values of $\text{Co}_3\text{Sn}_2\text{S}_2$ in ref. [26], independently of In content x . Sn atoms in $\text{Co}_3\text{Sn}_2\text{S}_2$ occupy two inequivalent Wyckoff positions, intra and inter Co Kagomé layer sites, and in the present study, Sn atoms at the inter-layer sites are substituted by In atoms for the proper description of the paramagnetic insulating phase at $x = 1.0$ [30]. We generate the maximally localized Wannier function to construct an effective tight-binding Hamiltonian from the obtained electronic structures with WANNIER90 package [33, 34] through the WIEN2WANNIER interface [35]. We explicitly include Co-3d, Sn/In-5s, 5p, and S-3p orbitals for the Wannier model. Based on the Wannier models, we investigate the intrinsic contributions to electric and thermoelectric transports, which are determined from purely electronic band structures, in $\text{Co}_3\text{In}_x\text{Sn}_{2-x}\text{S}_2$ by calculating the AHC and ANC with use of the following Kubo formulae [1, 36–38],

$$\sigma_{ab}^A(\mu, T) = -\frac{e^2}{\hbar} \int_{\text{BZ}} \frac{d\mathbf{k}}{(2\pi)^3} \sum_n f(\varepsilon_{n\mathbf{k}}) \Omega_{n,ab}(\mathbf{k}), \quad (2)$$

$$\alpha_{ab}^A(\mu, T) = \frac{ek_B}{\hbar} \int_{\text{BZ}} \frac{d\mathbf{k}}{(2\pi)^3} \sum_n s(\varepsilon_{n\mathbf{k}}) \Omega_{n,ab}(\mathbf{k}), \quad (3)$$

where e , k_B , \hbar and $\varepsilon_{n\mathbf{k}}$ are the positive elementary charge, Boltzmann constant, reduced Planck constant and one-particle energy with band index n and wave vector \mathbf{k} , respectively. The Fermi distribution function $f(\varepsilon)$ and the entropy density $s(\varepsilon)$ are given as $f(\varepsilon) = (e^{\frac{\varepsilon-\mu}{k_B T}} + 1)^{-1}$ and $s(\varepsilon) = -f(\varepsilon) \log f(\varepsilon) - [1 - f(\varepsilon)] \log [1 - f(\varepsilon)]$. $\Omega_{n,ab}(\mathbf{k})$ is the Berry curvature for band n , which is expressed as follows:

$$\Omega_{n,ab}(\mathbf{k}) = -2\hbar^2 \text{Im} \sum_{m(\neq n)} \frac{\langle n\mathbf{k} | v_a | m\mathbf{k} \rangle \langle m\mathbf{k} | v_b | n\mathbf{k} \rangle}{(\varepsilon_{n\mathbf{k}} - \varepsilon_{m\mathbf{k}})^2}, \quad (4)$$

where v_a is the velocity operator along a -direction, and $|n\mathbf{k}\rangle$ is the Bloch state with band index n and wave vector \mathbf{k} . In the actual numerical calculation, we perform the \mathbf{k} -integration in Eqs. (2) and (3) as the discrete \mathbf{k} -summation on 250^3 grids in the first Brillouin zone.

III. RESULTS

First, we show the results for $x = 0$, i.e., $\text{Co}_3\text{Sn}_2\text{S}_2$. Figure 1(a) shows the density of states (DOS) for $\text{Co}_3\text{Sn}_2\text{S}_2$ both in the paramagnetic and ferromagnetic states. The DOS in the paramagnetic state has a gap between -0.31 eV to -0.17 eV and the states from -0.17 eV to the Fermi energy E_F are occupied by one electron per unit cell, resulting in the fully-polarized magnetic moment $\sim 1\mu_B$ per unit cell in the ferromagnetic calculation. The exchange splitting pushes down

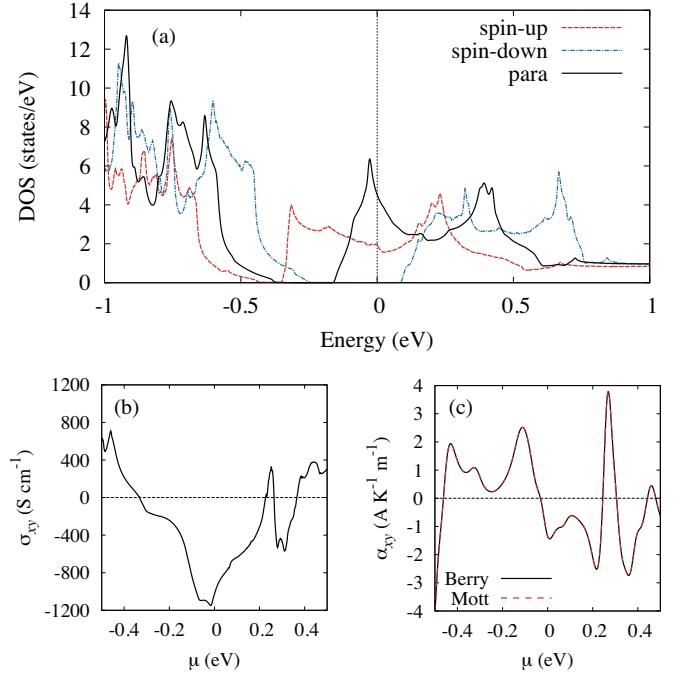


Figure 1. (a) DOS for $\text{Co}_3\text{Sn}_2\text{S}_2$ in paramagnetic and ferromagnetic states. The solid and dashed (dot-dashed) lines represent DOS per spin in the paramagnetic state and that with spin-up (down) in the ferromagnetic state, respectively. The chemical potential dependences of (b) AHC at $k_B T = 0$ and (c) ANC at $k_B T = 0.01$ eV. In panel (c), the solid and dashed lines represent the ANCs calculated via Berry phase formula in Eq. (3) and generalized Mott formula in Eq. (5), respectively.

the up-spin DOS, leading to the Fermi energy around the dip of the up-spin DOS, and pushes up the down-spin DOS, resulting the Fermi energy in a gap of down-spin DOS. As a consequence, the half-metallic state is realized.

The electric and thermoelectric transport properties in $\text{Co}_3\text{Sn}_2\text{S}_2$ are now discussed. Since the Berry curvature and ferromagnetic moment have the same symmetry properties under the magnetic point group, the AHC and ANC can be finite in the ferromagnetic state [37, 41–45]. In the present case, since the magnetic point group of the ferromagnetic phase is $\bar{3}m'$, only $\sigma_{xy}^A = -\sigma_{yx}^A$ and $\alpha_{xy}^A = -\alpha_{yx}^A$ can be finite and the other components vanish. It is instructive to rewrite ANC in Eq. (3) by the generalized Mott formula as follows [38],

$$\sigma_{ab}^A(\mu, T) = \frac{1}{eT} \int d\varepsilon (\varepsilon - \mu) \frac{\partial f}{\partial \varepsilon} \sigma_{ab}^A(\varepsilon, T = 0) \quad (5)$$

$$= -\frac{k_B}{e} \int d\varepsilon s(\varepsilon) \frac{\partial \sigma_{ab}^A(\varepsilon, T = 0)}{\partial \varepsilon}. \quad (6)$$

The well-known Mott relation is obtained as $\sigma_{ab}^A \sim -\frac{\pi^2 k_B^2 T}{3e} \frac{\partial \sigma_{ab}(\mu, T=0)}{\partial \mu}$, assuming that $\sigma_{ab}^A(\varepsilon, T = 0) \propto \varepsilon - \mu$ for $\varepsilon \sim \mu$ at low temperature limit.

Figures 1(b) and (c) display the μ dependence of AHC and ANC. A shift of the chemical potential corresponds to the rigid band picture, where $\mu > 0$ and $\mu < 0$ represent elec-

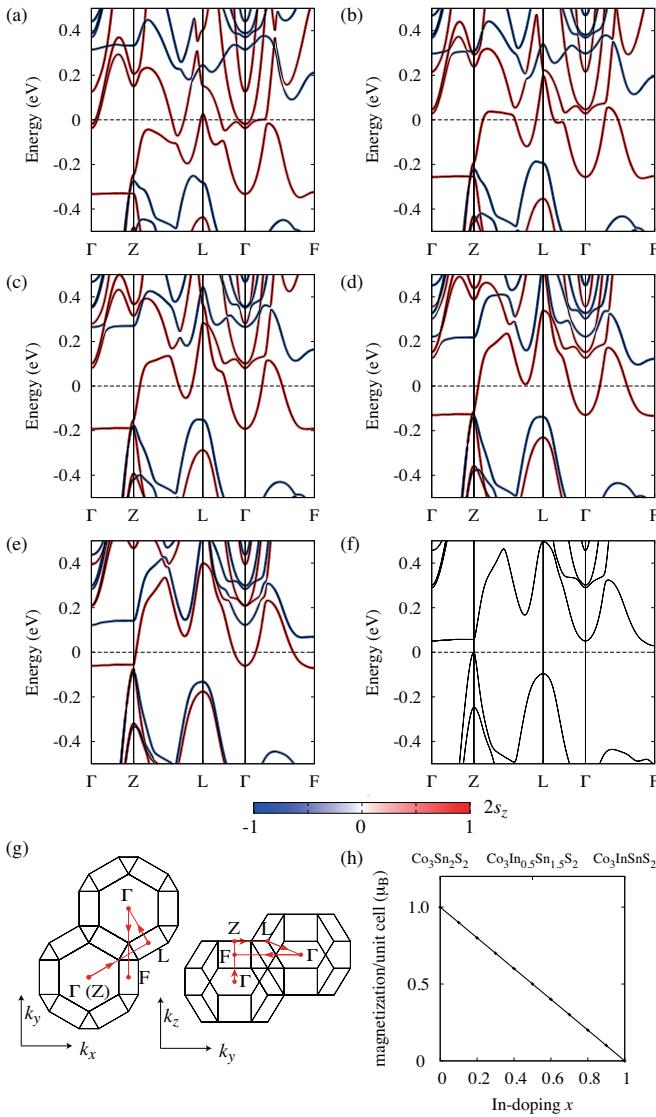


Figure 2. (a)-(f) Band structures for $\text{Co}_3\text{In}_x\text{Sn}_{2-x}\text{S}_2$ along high symmetry k -lines, where the color map represents the spin density along z -axis. (g) k -path on which the band structures are plotted in panels (a)-(f). (h) In-doping dependence of the net magnetization.

tron and hole dopings, respectively. Note that agreement of the ANCs calculated via Eqs. (3) and (5) is confirmed numerically as shown in Fig. 1(c). The calculated values of AHC and ANC are consistent with previous experimental and theoretical studies [6–8, 20, 21, 46]. Slight differences with previous theoretical calculations may come from the atomic position of S atoms which is optimized in refs. [6–8] while is adopted from the experimental value in the present study.

Focusing on the ANC for $\mu \leq 0$, one can see that the absolute value of the ANC is large at $\mu \sim 0$ and -0.113 eV with opposite signs. This implies that In-doping induces the sign change and/or the enhancement of the ANE as will be explicitly shown later. We also note that for qualitative understanding of the μ dependence of the ANC, the general-

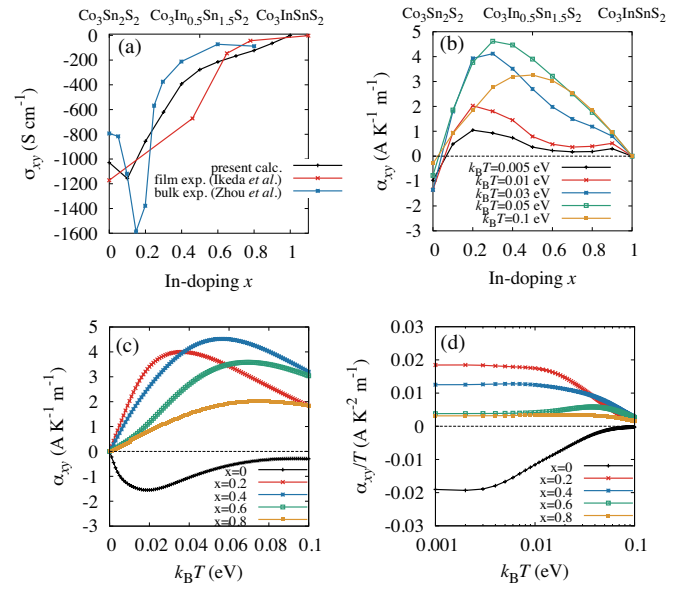


Figure 3. (a) Doping dependence of AHC σ_{xy}^A at $k_B T = 0$ and (b) that of ANC α_{xy}^A at finite temperatures. (c) Temperature dependence of α_{xy}^A and (d) that of α_{xy}^A/T at various In-doping concentrations. In panel (a), experimental data extracted from refs. [29, 39] are plotted together with calculated results for comparison.

ized Mott formula in Eq. (6) is useful. Since the entropy density $s(\varepsilon)$ is an even function with respect to $\varepsilon - \mu$ and rapidly decreases for $|\varepsilon - \mu| \gtrsim k_B T$, one can roughly estimate the sign and magnitude of the ANC from $\frac{\partial \sigma_{ab}(\varepsilon, T=0)}{\partial \varepsilon}$ for $|\varepsilon - \mu| \lesssim k_B T$. On one hand, around $\mu = 0$ eV, $\sigma_{ab}(\mu, T=0)$ shows steep increase as shown in Fig. 1(b) and the resulting ANC $\alpha_{xy}^A = -1.34 \text{ A K}^{-1} \text{ m}^{-1}$. On the other hand, around $\mu = -0.113$ eV, $\sigma_{ab}(\mu, T=0)$ shows steep decrease and the resulting ANC $\alpha_{xy}^A = 2.52 \text{ A K}^{-1} \text{ m}^{-1}$.

Next, let us move on to the In-doping dependence. The doping evolutions of the band structures and net magnetization are shown in Fig. 2. As mentioned before, in the non-doped case, the half-metallic state is realized and the DOS of the majority spin is metallic, while that of the minority spin has a gap. Hence, when Sn atoms are substituted by In atoms, most of holes are doped into majority spin states. The resulting magnetization decreases almost linearly with respect to the In content x and the system becomes paramagnetic insulator at $x = 1.0$ as shown in Fig. 2(h). These behaviors are qualitatively consistent with experimental results [25, 26] with slight difference of In-content at which paramagnetic insulating phase emerges. Correspondingly, the exchange splitting due to the magnetic ordering decreases with increasing x and the spin splitting of the band structure vanishes for $x = 1.0$ as shown in Figs. 2(a)-(f). The half-metallicity is retained in the whole investigated doping range, $x < 1.0$.

Results for the transport properties in $\text{Co}_3\text{In}_x\text{Sn}_{2-x}\text{S}_2$ are summarized in Fig. 3. Figures 3(a) and (b) show the doping dependence of the AHC and ANC. For slight hole doped region, the AHC increases with increasing x and reaches max-

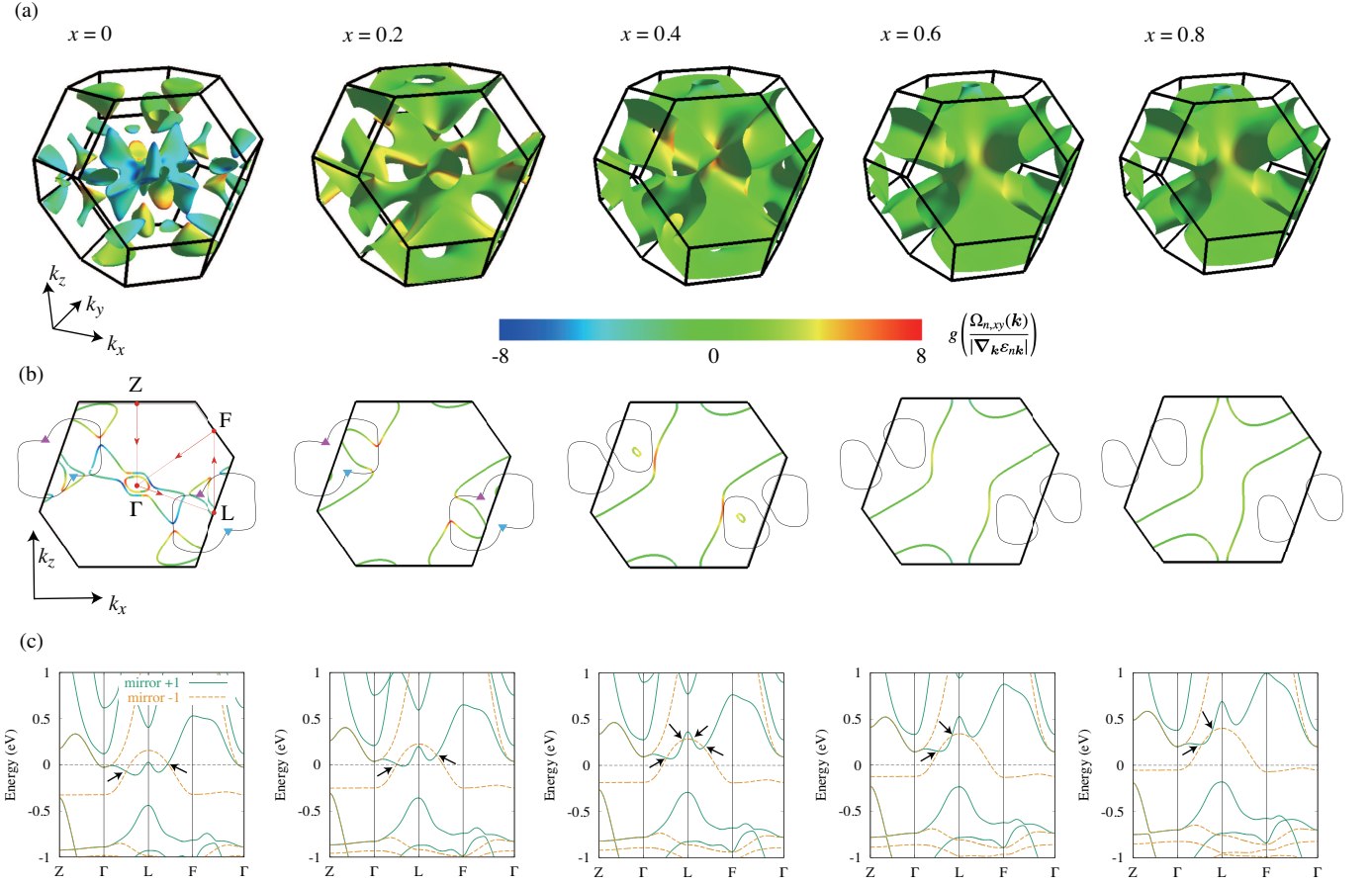


Figure 4. (a) Fermi surfaces for $\text{Co}_3\text{In}_x\text{Sn}_{2-x}\text{S}_2$, where the color map represents the intensity of $\frac{\Omega_{n,xy}(\mathbf{k})}{|\nabla_{\mathbf{k}}\varepsilon_{n\mathbf{k}}|}$ through the logarithmic function $g(x) \equiv \text{sgn}(x) \log(1 + |x|)$. (b) Those on k_x - k_z plane at $k_y = 0$. The black solid line represents the nodal lines in the absence of spin-orbit coupling. The upper (lower) triangles on the nodal lines denote the Weyl nodes with topological charge $+1$ (-1) in the presence of spin-orbit coupling. The \mathbf{k} -path along which band structures plotted in panel (c) is shown by red arrows in the left most panel. (c) Majority spin band structures in the absence of the spin-orbit coupling. The solid and dashed lines represent the energy bands with eigen values $+1$ and -1 of mirror symmetry operator on k_x - k_z plane, respectively. Band crossings corresponding to nodal lines are shown by arrows. Figures (a) and (b) are created with use of FERMISURFER code [40].

imum at $x \sim 0.1$. With further increasing x , the AHC decreases and vanishes at $x = 1.0$ where the system becomes paramagnetic (see also Fig. 2). The AHC sensitively depends on the electronic structure such as the details of the Fermi surfaces and the distribution of the Berry curvature in \mathbf{k} -space. As a result, the doping dependence of the AHC shows more complicated behavior than that of the magnetic moment [45, 47], which linearly decreases with respect to the doping concentration. As shown in Fig. 3(b), regarding the thermoelectric transport, the rigid band picture works well for the small doping region [see also Fig. 1(c)]. The ANC is negative at $x = 0$ and changes its sign into positive for the small doping content x . The absolute values of α_{xy}^A/T at low temperatures are large at $x \sim 0$ and 0.2 with values $|\alpha_{xy}^A|/T \sim 0.02 \text{ A K}^{-2} \text{ m}^{-1}$. The ANC decreases with further increasing x , reflecting the suppression of the magnetization. To elucidate the enhancement of the ANC for these doping concentrations, the temperature dependence of

the ANC is shown in Figs. 3(c) and (d). For large doping $x \geq 0.6$, α_{xy}^A shows linear T dependence in the wide temperature range $k_B T \lesssim 0.01 \text{ eV}$, while for $x = 0$ (0.2), that exhibits logarithmic T dependence for $0.005 \text{ eV} \lesssim k_B T \lesssim 0.04 \text{ eV}$ ($0.02 \text{ eV} \lesssim k_B T \lesssim 0.05 \text{ eV}$). These behaviors could be due to the stationary points in the nodal rings as demonstrated by Minami *et al.* in ref. [21].

In order to get clear insight into the low temperature behavior of the ANC, let us perform the detailed analysis of the topological properties of the electronic structures which are reflected in the Berry curvature $\Omega_{n,ab}(\mathbf{k})$. As mentioned before, the ANC is dominated by $\frac{\partial \sigma_{ab}(\varepsilon, T=0)}{\partial \varepsilon}$ for $|\varepsilon - \mu| \lesssim k_B T$, whose explicit form is given as follows [20],

$$\frac{\partial \sigma_{ab}^A(\varepsilon, T=0)}{\partial \varepsilon} = -\frac{e^2}{\hbar} \sum_n \int_{\varepsilon_{n\mathbf{k}}=\varepsilon} \frac{dS_{\mathbf{k}}}{(2\pi)^3} \frac{\Omega_{n,ab}(\mathbf{k})}{|\nabla_{\mathbf{k}}\varepsilon_{n\mathbf{k}}|}, \quad (7)$$

where $\int_{\varepsilon_{n\mathbf{k}}=\varepsilon} dS_{\mathbf{k}}$ represents the \mathbf{k} -integration over the isoenergy surfaces for $\varepsilon_{n\mathbf{k}} = \varepsilon$. From Eqs. (6) and (7), one can

see that the qualitative behavior of the ANC at low temperatures are governed by the distribution of the $\frac{\Omega_{n,ab}(\mathbf{k})}{|\nabla_{\mathbf{k}}\varepsilon_{n\mathbf{k}}|}$ near the Fermi surfaces. In Fig. 4(a), we show the Fermi surfaces with $\frac{\Omega_{n,ab}(\mathbf{k})}{|\nabla_{\mathbf{k}}\varepsilon_{n\mathbf{k}}|}$. The value of $\frac{\Omega_{n,ab}(\mathbf{k})}{|\nabla_{\mathbf{k}}\varepsilon_{n\mathbf{k}}|}$ is positive on the small portions of the Fermi surfaces for $x = 0$, while on more wide region, $\frac{\Omega_{n,ab}(\mathbf{k})}{|\nabla_{\mathbf{k}}\varepsilon_{n\mathbf{k}}|}$ becomes negative. As a result, the \mathbf{k} -integration over the Fermi surfaces of $\frac{\Omega_{n,ab}(\mathbf{k})}{|\nabla_{\mathbf{k}}\varepsilon_{n\mathbf{k}}|}$ is negative, resulting in $\alpha_{xy}^A < 0$ for $\text{Co}_3\text{Sn}_2\text{S}_2$ as shown in Fig. 3(b). On the other hand, for $x = 0.2$, the area of the Fermi surfaces on which $\frac{\Omega_{n,ab}(\mathbf{k})}{|\nabla_{\mathbf{k}}\varepsilon_{n\mathbf{k}}|}$ is negative becomes small and the resulting ANC is positive. The absolute value of $\frac{\Omega_{n,ab}(\mathbf{k})}{|\nabla_{\mathbf{k}}\varepsilon_{n\mathbf{k}}|}$ decreases with further increasing x , and the ANCs for large x have small values [see also Fig. 3(b)].

We here demonstrate that the intensity of the Berry curvature on Fermi surfaces is closely related to the nodal lines. As shown in Fig. 4(b), the nodal lines appear on the mirror symmetry planes in the absence of the spin-orbit coupling. The spin-orbit coupling gaps out the nodal lines but leaves the energy ~ 0.065 eV, resulting in the Weyl nodes for $x = 0$ [6, 7]. In this case, the energy bands characterized by different eigen values ± 1 of the mirror symmetry operator produce nodal lines due to its crossing [see Fig. 4(c)]. This origin of nodal lines is similar to those in archetypal nonmagnetic nodal line semimetals Ca_3P_2 [48, 49] and CaAgX ($X=\text{P}, \text{As}$) [50].

The hole doping decreases the Fermi energy and, as a result, shift the Weyl nodes away from the Fermi level. The nodal rings are located around the Fermi energy for small hole doping and for $x \lesssim 0.2$, the nodal lines surrounding the L-point cross the Fermi surfaces as shown in Fig. 4(b). The band at L-point near the Fermi energy with mirror eigen value $+1$ shifts upward in energy with increasing x and cross with the band having mirror eigen value -1 for $x \sim 0.3$, as shown in Fig. 4(c). Then, the nodal lines are split into two rings, as shown in Fig. 4(b), with the annihilation of Weyl nodes in the presence of the spin-orbit coupling. The nodal lines still cross the Fermi surfaces for $x < 0.4$ and give the significant contribution to the ANC. For $x \gtrsim 0.6$, the nodal lines are located far from the Fermi level, resulting in the small Berry curvature on the whole Fermi surfaces. One can clearly see that the intensity of the Berry curvature is large near the nodal lines.

IV. SUMMARY AND DISCUSSIONS

In the present paper, we investigated the magnetic and transport properties in $\text{Co}_3\text{In}_x\text{Sn}_{2-x}\text{S}_2$ based on first-principles calculations in which In-doping effect is treated within the virtual crystal approximation. We show that the anomalous Hall and Nernst conductivities show complicated behaviors with varying x against linearly reduced magnetization with respect to In content x due to the half-metallic electronic states. The Nernst conductivity has large values for $x \sim 0$ and 0.2 with opposite signs and show logarithmic temperature dependence consistently with the previous theoretical study [21]. We also clarify that the low temperature behavior of the anomalous Nernst conductivity can be understood by the distribution of the Berry curvature divided by the Fermi velocity. The close relationships between the Berry curvature, nodal rings, and anomalous Nernst effect are explicitly demonstrated. The intensity of the Berry curvature has a large value near the nodal rings for small hole doping, leading to a large anomalous Nernst conductivity. The In-doping induces the reconstruction of the nodal rings and moves the nodal lines far away from the Fermi level, resulting in the small Berry curvature on the Fermi surfaces. Our results give a qualitative understanding of the thermoelectric transport in $\text{Co}_3\text{In}_x\text{Sn}_{2-x}\text{S}_2$ and encourage experimental measurements of the anomalous Nernst effect in $\text{Co}_3\text{In}_x\text{Sn}_{2-x}\text{S}_2$.

Lastly, we comment on the important issues which are not addressed in this study. In the present paper, we have focused on the intrinsic contribution to the anomalous transports and neglected the extrinsic effects such as side-jump and skew-scattering [1]. Effects of the structural disorder, however, is inevitable in doped compounds in general and might give considerably large extrinsic contribution to the thermoelectric transport pointed by several authors [27, 51, 52]. A quantitative study on extrinsic contributions using first-principles calculations is a remaining issue in a future work.

ACKNOWLEDGMENTS

This research was supported by JSPS KAKENHI Grants Numbers JP15H05883 (J-Physics), JP18H04230, JP19H01842, JP20H01830, JP20H05262, JP20K05299, and JP20K21067. We also acknowledge supports from JST PRESTO Grant number JPMJPR17N8 and JST CREST Grant number JPMJCR18T2. A part of the numerical calculations was carried out using MASAMUNE-IMR of the Center for Computational Materials Science, Institute for Materials Research, Tohoku University. YY thanks H. Kusunose for sharing computer facilities.

[1] N. Nagaosa, J. Sinova, S. Onoda, A. H. MacDonald, and N. P. Ong, *Rev. Mod. Phys.* **82**, 1539 (2010).
 [2] D. Xiao, M.-C. Chang, and Q. Niu, *Rev. Mod. Phys.* **82**, 1959 (2010).

[3] N. P. Armitage, E. J. Mele, and A. Vishwanath, *Rev. Mod. Phys.* **90**, 015001 (2018).
 [4] Y. Tokura, K. Yasuda, and A. Tsukazaki, *Nat. Rev. Phys.* **1**, 126 (2019).

- [5] C. Fu, Y. Sun, and C. Felser, *APL Materials* **8**, 040913 (2020).
- [6] E. Liu, Y. Sun, N. Kumar, L. Muechler, A. Sun, L. Jiao, S.-Y. Yang, D. Liu, A. Liang, Q. Xu, J. Kroder, V. Süß, H. Borrmann, C. Shekhar, Z. Wang, C. Xi, W. Wang, W. Schnelle, S. Wirth, Y. Chen, S. T. B. Goennenwein, and C. Felser, *Nat. Phys.* **14**, 1125 (2018).
- [7] Q. Wang, Y. Xu, R. Lou, Z. Liu, M. Li, Y. Huang, D. Shen, H. Weng, S. Wang, and H. Lei, *Nat. Commun.* **9**, 3681 (2018).
- [8] S. N. Guin, P. Vir, Y. Zhang, N. Kumar, S. J. Watzman, C. Fu, E. Liu, K. Manna, W. Schnelle, J. Gooth, C. Shekhar, Y. Sun, and C. Felser, *Adv. Mater.* **31**, 1806622 (2019).
- [9] A. Sakai, Y. P. Mizuta, A. A. Nugroho, R. Sihombing, T. Koretsune, M.-T. Suzuki, N. Takemori, R. Ishii, D. Nishio-Hamane, R. Arita, P. Goswami, and S. Nakatsuji, *Nat. Phys.* **14**, 1119 (2018).
- [10] S. N. Guin, K. Manna, J. Noky, S. J. Watzman, C. Fu, N. Kumar, W. Schnelle, C. Shekhar, Y. Sun, J. Gooth, and C. Felser, *NPG Asia Mater.* **11**, 16 (2019).
- [11] R. Wehrich and I. Anusca, *Z. Anorg. Allg. Chem.* **632**, 1531 (2006).
- [12] M. Holder, Y. S. Dedkov, A. Kade, H. Rosner, W. Schnelle, A. Leithe-Jasper, R. Wehrich, and S. L. Molodtsov, *Phys. Rev. B* **79**, 205116 (2009).
- [13] W. Schnelle, A. Leithe-Jasper, H. Rosner, F. M. Schappacher, R. Pöttgen, F. Peilnhöfer, and R. Wehrich, *Phys. Rev. B* **88**, 144404 (2013).
- [14] K. Fujiwara, J. Ikeda, J. Shiogai, T. Seki, K. Takanashi, and A. Tsukazaki, *Jpn. J. Appl. Phys.* **58**, 050912 (2019).
- [15] D. F. Liu, A. J. Liang, E. K. Liu, Q. N. Xu, Y. W. Li, C. Chen, D. Pei, W. J. Shi, S. K. Mo, P. Dudin, T. Kim, C. Cacho, G. Li, Y. Sun, L. X. Yang, Z. K. Liu, S. S. P. Parkin, C. Felser, and Y. L. Chen, *Science* **365**, 1282 (2019).
- [16] L. Jiao, Q. Xu, Y. Cheon, Y. Sun, C. Felser, E. Liu, and S. Wirth, *Phys. Rev. B* **99**, 245158 (2019).
- [17] N. Morali, R. Batabyal, P. K. Nag, E. Liu, Q. Xu, Y. Sun, B. Yan, C. Felser, N. Avraham, and H. Beidenkopf, *Science* **365**, 1286 (2019).
- [18] H. Yang, W. You, J. Wang, J. Huang, C. Xi, X. Xu, C. Cao, M. Tian, Z.-A. Xu, J. Dai, and Y. Li, *Phys. Rev. Materials* **4**, 024202 (2020).
- [19] A. A. Burkov, *Phys. Rev. Lett.* **113**, 187202 (2014).
- [20] M. P. Ghimire, J. I. Facio, J.-S. You, L. Ye, J. G. Checkelsky, S. Fang, E. Kaxiras, M. Richter, and J. van den Brink, *Phys. Rev. Research* **1**, 032044 (2019).
- [21] S. Minami, F. Ishii, M. Hirayama, T. Nomoto, T. Koretsune, and R. Arita, *Phys. Rev. B* **102**, 205128 (2020).
- [22] X. Chen, M. Wang, C. Gu, S. Wang, Y. Zhou, C. An, Y. Zhou, B. Zhang, C. Chen, Y. Yuan, M. Qi, L. Zhang, H. Zhou, J. Zhou, Y. Yao, and Z. Yang, *Phys. Rev. B* **100**, 165145 (2019).
- [23] Z. Y. Liu, T. Zhang, S. X. Xu, P. T. Yang, Q. Wang, H. C. Lei, Y. Sui, Y. Uwatoko, B. S. Wang, H. M. Weng, J. P. Sun, and J.-G. Cheng, *Phys. Rev. Materials* **4**, 044203 (2020).
- [24] Z. Guguchia, J. A. T. Verezhak, D. J. Gawryluk, S. S. Tsirkin, J. X. Yin, I. Belopolski, H. Zhou, G. Simutis, S. S. Zhang, T. A. Cochran, G. Chang, E. Pomjakushina, L. Keller, Z. Skrzeczowska, Q. Wang, H. C. Lei, R. Khasanov, A. Amato, S. Jia, T. Neupert, H. Luetkens, and M. Z. Hasan, *Nat. Commun.* **11**, 559 (2020).
- [25] M. A. Kassem, Y. Tabata, T. Waki, and H. Nakamura, *J. Phys. Soc. Jpn.* **85**, 064706 (2016).
- [26] J. Corps, P. Vaqueiro, A. Aziz, R. Grau-Crespo, W. Kockelmann, J.-C. Jumas, and A. V. Powell, *Chem. Mater.* **27**, 3946 (2015).
- [27] J. Shen, Q. Zeng, S. Zhang, H. Sun, Q. Yao, X. Xi, W. Wang, G. Wu, B. Shen, Q. Liu, and E. Liu, *Adv. Funct. Mater.* **30**, 2000830 (2020).
- [28] G. S. Thakur, P. Vir, S. N. Guin, C. Shekhar, R. Wehrich, Y. Sun, N. Kumar, and C. Felser, *Chem. Mater.* **32**, 1612 (2020).
- [29] H. Zhou, G. Chang, G. Wang, X. Gui, X. Xu, J.-X. Yin, Z. Guguchia, S. S. Zhang, T.-R. Chang, H. Lin, W. Xie, M. Z. Hasan, and S. Jia, *Phys. Rev. B* **101**, 125121 (2020).
- [30] J. Rothballe, F. Bachhuber, S. M. Rommel, T. Söhnle, and R. Wehrich, *RSC Adv.* **4**, 42183 (2014).
- [31] P. Blaha, K. Schwarz, G. Madsen, D. Kvasnicka, and J. Luitz, An augmented plane wave + local orbitals program for calculating crystal properties (Technische Universität Wien Vienna, 2001).
- [32] P. Blaha, K. Schwarz, F. Tran, R. Laskowski, G. K. H. Madsen, and L. D. Marks, *J. Chem. Phys.* **152**, 074101 (2020).
- [33] N. Marzari, A. A. Mostofi, J. R. Yates, I. Souza, and D. Vanderbilt, *Rev. Mod. Phys.* **84**, 1419 (2012).
- [34] G. Pizzi, V. Vitale, R. Arita, S. Blügel, F. Freimuth, G. Géranton, M. Gibertini, D. Gresch, C. Johnson, T. Koretsune, J. Ibañez-Azpiroz, H. Lee, J.-M. Lihm, D. Marchand, A. Marrazzo, Y. Mokrousov, J. I. Mustafa, Y. Nohara, Y. Nomura, L. Paulatto, S. Poncé, T. Ponweiser, J. Qiao, F. Thöle, S. S. Tsirkin, M. Wierzbowska, N. Marzari, D. Vanderbilt, I. Souza, A. A. Mostofi, and J. R. Yates, *J. Phys.: Condens. Matter* **32**, 165902 (2020).
- [35] J. Kuneš, R. Arita, P. Wissgott, A. Toschi, H. Ikeda, and K. Held, *Comput. Phys. Commun.* **181**, 1888 (2010).
- [36] F. D. M. Haldane, *Phys. Rev. Lett.* **93**, 206602 (2004).
- [37] X. Wang, J. R. Yates, I. Souza, and D. Vanderbilt, *Phys. Rev. B* **74**, 195118 (2006).
- [38] D. Xiao, Y. Yao, Z. Fang, and Q. Niu, *Phys. Rev. Lett.* **97**, 026603 (2006).
- [39] The $\text{Co}_3\text{In}_x\text{Sn}_{2-x}\text{S}_2$ films were grown on Al_2O_3 (0001) substrates by co-sputtering [14]. The c -axis oriented growth was confirmed by X-ray diffraction measurements. The thicknesses of the films were approximately 40 nm. After cooling the samples in an out-of-plane magnetic field of 1 T, the electrical transport properties were measured at 2 K. σ_{xy} was calculated by $\sigma_{xy} = \rho_{yx} / (\rho_{xx}^2 + \rho_{yx}^2)$, where ρ_{xx} is electrical resistivity and ρ_{yx} is Hall resistivity. The detailed transport properties will be reported elsewhere.
- [40] M. Kawamura, *Comput. Phys. Commun.* **239**, 197 (2019).
- [41] R. R. Birss, *Symmetry and Magnetism* (North-Holland, Amsterdam, 1964).
- [42] M. Seemann, D. Ködderitzsch, S. Wimmer, and H. Ebert, *Phys. Rev. B* **92**, 155138 (2015).
- [43] H. Watanabe and Y. Yanase, *Phys. Rev. B* **98**, 245129 (2018).
- [44] S. Hayami, M. Yatsushiro, Y. Yanagi, and H. Kusunose, *Phys. Rev. B* **98**, 165110 (2018).
- [45] M.-T. Suzuki, T. Koretsune, M. Ochi, and R. Arita, *Phys. Rev. B* **95**, 094406 (2017).
- [46] A. Ozawa and K. Nomura, *J. Phys. Soc. Jpn.* **88**, 123703 (2019).
- [47] M. Naka, S. Hayami, H. Kusunose, Y. Yanagi, Y. Motome, and H. Seo, *Phys. Rev. B* **102**, 075112 (2020).
- [48] L. S. Xie, L. M. Schoop, E. M. Seibel, Q. D. Gibson, W. Xie, and R. J. Cava, *APL Mater.* **3**, 083602 (2015).
- [49] Y.-H. Chan, C.-K. Chiu, M. Y. Chou, and A. P. Schnyder, *Phys. Rev. B* **93**, 205132 (2016).
- [50] A. Yamakage, Y. Yamakawa, Y. Tanaka, and Y. Okamoto, *J. Phys. Soc. Jpn.* **85**, 013708 (2016).
- [51] L. Ding, J. Koo, L. Xu, X. Li, X. Lu, L. Zhao, Q. Wang, Q. Yin, H. Lei, B. Yan, Z. Zhu, and K. Behnia, *Phys. Rev. X* **9**, 041061 (2019).

[52] M. Papaj and L. Fu, arXiv:2008.07974 (2020).